Submitted to ApJ.

Tomographic Separation of Composite Spectra. IX. The Massive Close Binary HD 115071

Laura R. Penny[1]

Department of Physics and Astronomy
College of Charleston
Charleston, SC 29424;
pennyl@cofc.edu

Douglas R. Gies[2]

Center for High Angular Resolution Astronomy and
Department of Physics and Astronomy
Georgia State University, Atlanta, GA 30303;
gies@chara.gsu.edu

John H. Wise[3]

School of Physics
Georgia Institute of Technology
Atlanta, GA 30332;
jwise@astro.psu.edu

D. J. Stickland, C. Lloyd

Rutherford Appleton Laboratory
Chilton, Didcot, Oxon, OX11 0QX, United Kingdom;
ds@astro1.bnsc.rl.ac.uk, cxl@ast.star.rl.ac.uk

ABSTRACT

[1]Guest Observer, Complejo Astronomico El Leoncito (CASLEO), San Juan, Argentina

[2]Guest Observer, Mount Stromlo and Siding Springs Observatories, Australia

[3]Current address: Department of Astronomy and Astrophysics, Pennsylvania State University, 532 Davey Laboratory, University Park, PA 16802

We present the first orbital elements for the massive close binary, HD 115071, a double-lined spectroscopic binary in a circular orbit with a period of 2.73135 ± 0.00003 days. The orbital semiamplitudes indicate a mass ratio of $M_2/M_1 = 0.58 \pm 0.02$ and yet the stars have similar luminosities. We used a Doppler tomography algorithm to reconstruct the individual component optical spectra, and we applied well known criteria to arrive at classifications of O9.5 V and B0.2 III for the primary and secondary, respectively. We present models of the *Hipparcos* light curve of the ellipsoidal variations caused by the tidal distortion of the secondary, and the best fit model for a Roche-filling secondary occurs for an inclination of $i = 50°$. The maximum masses are $11M_\odot$ and $6M_\odot$ for the primary and secondary, respectively, so that both stars are very overluminous for their mass. We suggest that the system has recently emerged from extensive Case A mass transfer.

Subject headings: binaries: spectroscopic — stars: early-type — stars: evolution — stars: individual (HD 115071)

1. Introduction

The hot, massive star, HD 115071 (V961 Cen, LS 2998, HIC 64737), is found in the sky close to the open cluster, Stock 16 (Turner 1985), and is classified as O9.5 V by Houk & Cowley (1975) and B0.5 Vn by Garrison et al. (1977). The star is not a known visual binary (Mason et al. 1998) but early measurements by spectroscopists indicated it is radial velocity variable and a probable spectroscopic binary (Cruz-González et al. 1974; Conti et al. 1977). The proof of its binary nature came relatively recently in studies by Penny (1996) and Howarth et al. (1997). Both papers presented a cross-correlation analysis of a single, high dispersion, UV spectrum made with the *International Ultraviolet Explorer Satellite* (*IUE*) that demonstrated that the system is in fact a double-lined binary. Stickland & Lloyd (2001) measured the radial velocities of the components in this spectrum and proposed an orbital period of 2.73126 d based upon a light curve constructed from *Hipparcos* photometry. Lloyd & Stickland (2001) present a model of the light curve, and they argue that the system has evolved through Case A mass transfer.

The details and outcomes of Case A Roche lobe overflow in massive binaries are still subjects of considerable debate (Wellstein et al. 2001), and thus, the orbital and physical parameters of a system like HD 115071 are of great interest. Here we present the first double-lined orbital solution for the binary (§3) based upon new high quality optical spectra. We apply a version of the Doppler tomography algorithm (which we have used to good effect

with UV spectra in prior papers in this series) to reconstruct the individual spectra of both components, from which we determine the spectral classifications, projected rotational velocities, and flux ratio (§4). We also present a light curve analysis constrained by the spectroscopic results that allows us to place limits on the stellar masses (§5). These masses are much lower than expected, and we discuss the evolutionary implications in §6.

2. Observations and Reductions

Our spectra were obtained in two observing runs at different sites. The first set was obtained with the 2.15-m telescope of the Complejo Astronomico El Leoncito (CASLEO) and REOSC echelle spectrograph (on loan from the Institut d'Astrophysique, Universite de Liege, Belgium) during the period 1997 March 19 – 28. The REOSC spectrograph uses an echelle grating with 70 grooves mm^{-1} and blazed at 226434 Å together with a cross disperser grating of 400 grooves mm^{-1} blazed at 4000 Å. The detector was a TEK 1024×1024 CCD with 24μm square pixels used with a gain of 1.98 e^-/ADU (read noise of 7.4 e^-). We used a 200μm slit that corresponds to 2″ on the sky. This arrangement produced an echellogram from which we extracted 23 orders, spanning the range from 3575 to 5700 Å with a spectral resolution of $\lambda/\Delta\lambda = 13000$. We usually obtained 3 exposures of 660 s duration that were later co-added in software to improve the S/N ($\approx$ 150 per pixel in the better exposed portions of the spectrum). Numerous bias, flat field, dark, and Th-Ar comparison images were obtained each night.

Our second observing run took place at the 74-inch telescope at Mount Stromlo Observatory over the period 1998 April 6 – 14. These spectra were made with the coude spectrograph using grating C (600 grooves per mm, blazed at 12500Å in first order) in third order with a BG12 order sorting filter. The detector was a SITe CCD (D14) with 15 μm square pixels in a 4096×2048 format. This arrangement produced single order spectra that covered the range 3804 – 4220 Å with a reciprocal dispersion of 0.10 Å per pixel and a resolution element of 0.30 Å FWHM ($\lambda/\Delta\lambda = 13400$). Exposure times were usually 45 minutes, and the final spectra have a typical S/N = 160 per pixel in the continuum.

The spectra were reduced using standard routines in IRAF[4]. The echelle spectra were traced, extracted, and wavelength calibrated using the task *doecslit*, and the extracted orders were rectified to a unit continuum by fitting a high order spline function to line-free regions

[4]IRAF is distributed by the National Optical Astronomy Observatories, which is operated by the Association of Universities for Research in Astronomy, Inc., under cooperative agreement with the National Science Foundation.

(using the task *continuum*). Finally the individual orders were linked together with the task *scombine*. Small amplitude irregularities related to the fitting of the echelle blaze function were removed through a comparison of the same in spectra of the narrow-lined B-star, τ Sco, which was also observed each night. Similar procedures were followed with the MSO coude spectra, and the single-orders were extracted and calibrated with the task *doslit*. The spectra from each run were then collected and transformed onto their respective heliocentric wavelength grids.

3. Radial Velocities and Orbital Elements

Our procedure for measuring radial velocities in *IUE* spectra (Penny et al. 1997) involves fitting Gaussians to the cross-correlation functions of the target spectrum with a narrow-lined reference spectrum. The optical spectra we consider here have many fewer stellar lines and much better S/N than the *IUE* spectra, so we revised our techniques accordingly. First, we fit each absorption feature separately rather than fitting the entire spectrum through one cross-correlation measurement. Secondly, we made the fit of the composite profiles using spectral templates rather than Gaussian functions (since the lines have shapes dominated by linear Stark broadening or rotational broadening). The templates were formed from spectra we obtained during each run of the star, HD 57682 (O9 IV; Walborn (1972)). This star is a reasonable match in classification to both components in HD 115071 (§4), but has narrower lines ($V \sin i = 33$ km s^{-1}; Penny (1996)). The radial velocity of this star was measured by Gaussian fitting of lines taken from the list of Bolton & Rogers (1978), and we found an average radial velocity of 25.0±0.5 and 26.0±1.1 km s^{-1} from the CASLEO and MSO spectra, respectively. The averaged template spectra from each run were shifted by these values to place them in the rest frame. Next, we artificially broadened each template spectrum by convolution with a rotational broadening function to produce profiles that matched the spectral components of HD 115071 in the best separated quadrature spectra. We also used these resolved profiles to estimate the line depth ratio between the components. Once these fitting parameters were set, we determined the radial velocities of each component for a given line by a least-squares fit of the shifts required for each template. This approach provided good fits of the observed profiles for all but two cases (HJD 2,450,529.792 and 2,450,531.755) where the line depth ratio appeared to be reversed.

We used this technique to measure radial velocities for the strongest lines in the spectrum, specifically H I $\lambda\lambda$3835, 3889, 3970, 4101, 4340, 4861, He I $\lambda\lambda$3819, 4009, 4026, 4121, 4143, 4387, 4471, 4921, 5015, He II λ4686, and Si IV λ4089. There was no evidence of systematic line-to-line differences in the radial velocity measurements, and so no line specific

corrections were applied. The radial velocities from all the available lines were averaged together after deletion of any very discrepant measurements. Finally, we made small adjustments to these averages based on measurements of the strong interstellar Ca II $\lambda\lambda 3933, 3968$ lines. An interstellar spectrum was formed by extracting the mean spectrum in the immediate vicinity of each interstellar absorption line. We then cross correlated this spectrum with each individual spectrum to measure any small deviations in our wavelength calibration (generally < 3 km s^{-1}), and these small corrections were applied to the mean velocities. We found the radial velocity of the interstellar Ca II lines was -17.0 ± 0.2 and -16.0 ± 0.2 km s^{-1} for the CASLEO and MSO spectra, respectively. Table 1 lists the heliocentric dates of mid-observation, orbital phase, and for each component, the mean radial velocity, the standard deviation of the mean, the observed minus calculated residual from the orbital fit, and the number of lines used in the mean. Table 1 also gives the radial velocities from the single *IUE* spectrum measured by Stickland & Lloyd (2001) (adjusted for the ISM velocity on the MSO system).

Stickland & Lloyd (2001) and Lloyd & Stickland (2001) found that the *Hipparcos* light curve was best fit with a double sine, ellipsoidal variation for an orbital period $P = 2.73126 \pm 0.00009$ d. We found that this period also agreed reasonably well with our radial velocity data. We used the non-linear, least-squares fitting program of Morbey & Brosterhus (1974) to solve for the period and other orbital elements for the primary (the more luminous and massive star) and secondary components separately, and this yielded period estimates of 2.73149 ± 0.00007 and 2.73138 ± 0.00015 d, respectively. We made one additional calculation of the period by dividing the difference between the best fit time of the *Hipparcos* photometry maximum and our spectroscopically determined time of quadrature by the closest integral number of cycles, and this led to a period of 2.73130 ± 0.00004 d. We adopted the error weighted mean of these estimates for our working value of the period, $P = 2.73135 \pm 0.00003$ d.

We fixed this period and then fit for the remaining orbital elements independently for both components. The fitted epoch of primary maximum velocity, T_0, was the same within errors for both solutions, and so we applied the mean value to fits of both components. Eccentric solutions produced estimates of eccentricity consistent with a value of zero, and our final solutions in Table 2 assume circular motion. The observed and calculated radial velocity curves appear in Figure 1. The only major discrepancies occur in the *IUE* measurements (not used in the solution), both of which are ≈ 38 km s^{-1} above the predicted curve. Note that in the case of the primary, the *IUE* velocity falls well above the maximum for the entire curve, so the mismatch cannot be due to an incorrect orbital phase for example. The systematic difference may be related to line formation at different heights in an expanding atmosphere or orbital motion about a distant, unseen, tertiary star.

4. Tomographic Reconstruction

We used the Doppler tomography algorithm described by Bagnuolo et al. (1994) to reconstruct the individual primary and secondary spectra independently from the CASLEO and MSO spectra. We took the radial velocity shifts for each component from the orbital solutions in Table 2, then the reconstruction was run for 50 iterations with a gain of 0.8 (the results are insensitive to both parameters). The reconstructed spectra are plotted in in Figure 2 in a format similar to that used in the spectral atlas of Walborn & Fitzpatrick (1990). The reconstructions from the MSO spectra are shown just above those from the CASLEO spectra (in the short wavelength portion of Fig. 2), and there is good agreement between these two sets of spectra.

We compared the reconstructed spectra with the spectrum standards in the atlas of Walborn & Fitzpatrick (1990) to determine the spectral classifications of the components. The strengths of the He I $\lambda\lambda 4026, 4143, 4387$ lines relative to those of He II $\lambda\lambda 4200, 4541$ are all consistent with a spectral type of O9.5 for the primary. The ratio of the Si IV $\lambda\lambda 4088, 4116$ lines to the nearby He I $\lambda\lambda 4121, 4143$ features indicate a main sequence class, as does the relatively strong He II $\lambda 4686$ to He I $\lambda 4713$ ratio. Thus, we classify the primary as type O9.5 V, and we compare its spectrum in Figure 2 to that of HD 93027, which is given as the standard of this class in Walborn & Fitzpatrick (1990).

The secondary, on the other hand, has features indicating a cooler temperature and later type. The ratio of Si III $\lambda 4552$ to Si IV $\lambda 4088$ has a good match in the interpolated type B0.2 introduced by Walborn & Fitzpatrick (1990). The relative strength of the Si IV $\lambda\lambda 4088, 4116$ lines compared to the neighboring He I $\lambda\lambda 4121, 4143$ features clearly leads to a luminosity class III. Figure 2 illustrates the good agreement between the spectrum of the secondary and HD 108639 that Walborn & Fitzpatrick (1990) use as a standard for type B0.2 III.

The two spectral standards, HD 93027 and HD 108639, provided us with the means to estimate the visual flux ratio, $r = F_2/F_1$, by matching the line depths in the reconstructed spectra with those in the standards. This was done by aligning the reconstructed and standard spectra, adjusting for differences in the placement of the continuum, Gaussian smoothing of the spectra to eliminate differences in projected rotational velocity and instrumental broadening, and then finding a best fit line ratio that allocates a proportion of flux to each component to best match the line depths. We found $r = 0.92 \pm 0.12$ and 1.00 ± 0.12 for the MSO and CASLEO reconstructions, respectively, and we adopted the mean result, $r = 0.96 \pm 0.08$, in the light curve analysis below (§5).

Finally, we used the profiles in the reconstructed spectra to estimate the projected

rotational velocities of the components. We focused on the Si IV λ4088 profile for this purpose since it represents the strongest metallic line (intrinsically narrow) in the range covered by the MSO spectra. Our procedure involved calculating a grid of rotational broadening functions for a linear limb darkening law (Wade & Rucinski 1985; Gray 1992) and then convolving an observed narrow-lined spectrum with these broadening functions. We compared the spectral reconstructions from the MSO spectra with broadened versions of MSO spectra of the narrow-lined stars HD 53682 (O9 IV) and τ Sco (B0.2 V). The best fitting profile matches were made with $V \sin i = 101 \pm 10$ and 132 ± 15 km s^{-1} for the primary and secondary, respectively. These agree within errors with estimates from the *IUE* observation (Penny 1996; Howarth et al. 1997; Lloyd & Stickland 2001).

5. Light Curve Analysis and Masses

Lloyd & Stickland (2001) presented an analysis of the *Hipparcos* light curve (Perryman 1997), and here we update their work by restricting a number of the fitting parameters based upon the new spectroscopic results. We used the light curve synthesis code GENSYN (Mochnacki & Doughty 1972) to produce model V-band differential light curves (almost identical to differential *Hipparcos Hp* magnitudes for hot stars). The orbital parameters were taken from the spectroscopic solution, and the physical parameters were estimated from the spectral classifications of the stars. We set the stellar temperatures and gravities according to the spectral classification calibration of Howarth & Prinja (1989) for the primary ($T_{\rm eff\ 1} = 32$ kK, $\log g_1 = 3.9$), and for the secondary, we used data for comparable stars in the compilation of Underhill & Doazan (1982) ($T_{\rm eff\ 2} = 29$ kK, $\log g_2 = 3.6$). We then estimated the physical fluxes and limb darkening coefficients from tables in Kurucz (1994) and Wade & Rucinski (1985), respectively. We also used the Kurucz flux models to transform our observed 4000 Å flux ratio into a V-band flux ratio, $F_2/F_1 = 0.97 \pm 0.12$. The theoretical and observed flux ratios together yield an estimate of the ratio of stellar radii, $R_2/R_1 = 1.07 \pm 0.07$. Each trial run of GENSYN was set by two independent parameters, the system inclination i and primary polar radius (with the secondary radius set so that the orbital average flux ratio matched the observed flux ratio).

The observed light curve (Fig. 3) is a double-sine wave caused by tidal distortion in the stars. Since the stars have similar radii but the secondary has a much lower mass (§3), the secondary must be much closer to filling its critical Roche radius, so that the tidal generation of the light curve is due mainly to the distortion of the secondary. The amplitude of the photometric variation is proportional to the degree of tidal distortion (how close the secondary comes to filling its Roche volume) and to the sine of the inclination (maximal

effect for $i = 90°$). Our first fit of the light curve assumed that the secondary is very close to Roche-filling, and so this solution corresponds to the minimum inclination. This fit is shown as the solid line in Figure 3 for an inclination $i = 50°$. Models with a smaller secondary and less tidal distortion require a higher inclination to match the observations, and the dashed line in Figure 3 illustrates a model for $i = 64°$ and a radius, $R_2/R_\odot = 4.9$ ($\approx 82\%$ of the critical Roche radius). This fit is less satisfactory than the Roche-filling model, because the light curve at this inclination begins to show evidence of eclipses. Eclipses as subtle as those shown in Figure 3 are probably not ruled out by the *Hipparcos* photometry, but in higher inclination models the eclipses become so prominent and the light curve differs so much from the observations that such models can safely be ruled out. Thus, the allowed inclination range is $50° - 64°$. The stellar parameters associated with this range are collected in Table 3.

If the stars are synchronously rotating, then the projected rotational velocities would be $V \sin i = 99$ and 109 km s^{-1} for the primary and secondary, respectively, in the Roche-filling model (or 77 and 84 km s^{-1} in the under-filling model shown in Fig. 3). The observed projected rotational velocities are only slightly larger than these values. It would surprising if synchronous rotation did not occur in such a short period system, and so we prefer the Roche-filling model that provides a better match to the observed projected rotational velocities. The system absolute magnitude in the Roche-filling case is estimated as $M_V = -4.57$, and, for $V = 7.94$ and $E(B - V) = 0.50$ (Turner 1985), we estimate a distance of 1.5 ± 0.2 kpc (smaller than but comparable to the distance of 1.9 kpc for the cluster Stock 16; Turner (1985)).

6. Discussion

The first striking result from our analysis is the very low mass we find for both components. The stars have temperatures and luminosities that are associated with masses of 18 and $15 M_\odot$ for the primary and secondary, respectively, in the single star evolutionary tracks calculated by Schaller et al. (1992). (These estimates would be slightly reduced using evolutionary models that include rotation; Heger & Langer (2000), Meynet & Maeder (2000).) The secondary, in particular, has a luminosity characteristic of a star more than twice as massive than the upper limit we find (Table 3).

The second remarkable fact is that the secondary star has a spectral classification indicating it has evolved away from the main sequence. Thus, HD 115071 presents the classical "Algol paradox" that the lower mass component is the more evolved one, and we suggest the same solution of the paradox holds here as well, i.e., that the evolved component was originally the more massive object, but suffered significant mass transfer to its neighbor.

The theoretical models of binary evolution by Wellstein et al. (2001) offer some guidance in the interpretation of our results. Wellstein et al. (2001) describe the evolution of several very close systems that begin Roche lobe overflow during core H-burning (Case A). One case (their No. 31) has a $12.0M_{\odot}$ and $7.5M_{\odot}$ pair enter into a phase of rapid mass transfer (lasting some 300,000 years) that reverses the mass ratio and results in components of mass $3.9M_{\odot}$ and $15.5M_{\odot}$. These are comparable to the masses we find in HD 115071. Their models also suggest that the mass gainer only grows moderately in radius as the result of mass transfer (see their Fig. 7) in agreement with our results for the primary. However, other predictions about the post-mass transfer binary do not find confirmation in our results. Wellstein et al. (2001) suggest that the mass donor will be much fainter at the conclusion of Case A mass transfer whereas we find that the components are quite comparable in luminosity. Wellstein et al. (2001) also predict that the system period should become much larger after the mass ratio has reversed. For example, their model binary that began with a 2.5 d period ends up with a 7.99 d period at the conclusion of Case A mass transfer. Since HD 115071 is already one of the shortest period binaries known among O-stars (Mason et al. 1998), it is hard to imagine that its orbital period has increased significantly.

We suggest that these problems may be partially resolved if the system has only recently completed the rapid phase of mass transfer. If so, there has been little time for the system to expand with continuing mass transfer, and the orbital period could still be as low as the 2.73 d value we find. The best fit of the light curve suggests that the secondary is close to Roche-filling, and so the system may still be experiencing active mass transfer. Observations of any Hα emission (Thaller 1997) or IR excess (Gehrz et al. 1995) would provide valuable clues about the mass loss and/or mass transfer processes that might be occurring presently in this exceptional binary system.

We thank the staffs of CASLEO and MSO for their assistance in making these observations. Institutional support for L.R.P. has been provided from the College of Charleston School of Sciences and Mathematics. Additional support for L.R.P. was provided by the South Carolina NASA Space Grant Program and NSF grant AST-9528506. Institutional support for D.R.G. has been provided from the GSU College of Arts and Sciences and from the Research Program Enhancement fund of the Board of Regents of the University System of Georgia, administered through the GSU Office of the Vice President for Research. We gratefully acknowledge all this support.

REFERENCES

Bagnuolo, W. G., Jr., Gies, D. R., Hahula, M. E., Wiemker, R., & Wiggs, M. S. 1994, ApJ, 423, 446

Bolton, C. T., & Rogers, G. L. 1978, ApJ, 222, 234

Conti, P. S., Leep, E. M., & Lorre J. J. 1977, ApJ, 214, 759

Cruz-González, C., Recillas-Cruz, E., Costero, R., Peimbert, M., & Torres-Peimbert, S. 1974, Revista Mexicana Astr. Astrof., 1, 211

Garrison, R. F., Hiltner, W. A., & Schild, R. E. 1977, ApJS, 35, 111

Gehrz, R. D., et al. 1995, ApJ, 439, 417

Gray, D. F. 1992, The Observation and Analysis of Stellar Photospheres (2nd ed.) (Cambridge: Cambridge Univ. Press)

Heger, A., & Langer, N. 2000, ApJ, 544, 1016

Houk, N., & Cowley, A. P. 1975, Catalogue of two dimensional spectral types for the HD stars, Vol. 1 (Ann Arbor: Univ. Michigan)

Howarth, I. D., & Prinja, R. K. 1989, ApJS, 69, 527

Howarth, I. D., Siebert, K. W., Hussain, G. A. J., & Prinja, R. K. 1997, MNRAS, 284, 265

Kurucz, R. L. 1994, Solar Abundance Model Atmospheres for 0, 1, 2, 4, 8 km/s, Kurucz CD-ROM No. 19 (Cambridge, MA: Smithsonian Astrophysical Obs.)

Lloyd, C., & Stickland, D. J. 2001, A&A, 370, 1026

Mason, B. D., Gies, D. R., Hartkopf, W. I., Bagnuolo, W. G., Jr., ten Brummelaar, T., & McAlister, H. A. 1998, AJ, 115, 821

Meynet, G., & Maeder, A. 2000, A&A, 361, 101

Mochnacki, S. W., & Doughty, N. A. 1972, MNRAS, 156, 51

Morbey, C. L., & Brosterhus, E. B. 1974, PASP, 86, 455

Penny, L. R. 1996, ApJ, 463, 737

Penny, L. R., Gies, D. R., & Bagnuolo, W. G., Jr. 1997, ApJ, 483, 439

Perryman, M. A. C. 1997, The Hipparcos and Tycho Catalogues, ESA SP-1200 (ESA/ESTEC, Noordwijk)

Schaller, G., Schaerer, D., Meynet, G., & Maeder, A. 1992, A&AS, 96, 269

Stickland, D. J., & Lloyd, C. 2001, Observatory, 121, 1

Thaller, M. L. 1997, ApJ, 487, 380

Turner, D. G. 1985, ApJ, 292, 148

Underhill, A., & Doazan, V. (eds.) 1982, B Stars With and Without Emission Lines (NASA SP-456) (Washington, DC: NASA)

Wade, R. A., & Rucinski, S. M. 1985, A&AS, 60, 471

Walborn, N. R. 1972, AJ, 77, 312

Walborn, N. R., & Fitzpatrick, E. L. 1990, PASP, 102, 379

Wellstein, S., Langer, N., & Braun, H. 2001, A&A, 369, 939

AAS LaTeX macros v5.0.

Fig. 1.— The radial velocity measurements (*primary – filled circles; secondary – open circles*) and orbital solution (*solid lines*) plotted against orbital phase. Phase zero corresponds to the time of primary maximum radial velocity. The two plus marks show the *IUE* measurements that were not used in the solution.

Fig. 2.— A comparison of the reconstructed MSO spectra (*above*) and CASLEO spectra (*below*) of the primary and secondary with spectra of the same classifications from Walborn & Fitzpatrick (1990). All the spectra were Gaussian smoothed to a nominal resolution of 1.2 Å FWHM for consistent line broadening.

Fig. 3.— The *Hipparcos* light curve plotted against spectroscopic orbital phase. The solid line shows the predicted curve for a secondary Roche-filling model with $i = 50°$, while the dashed line represents the prediction for an under-filling model with $i = 64°$.

Table 1. Radial Velocity Measurements

HJD (-2,400,000)	Orbital Phase	V_1 (km s^{-1})	σ_1 (km s^{-1})	$(O-C)_1$ (km s^{-1})	n_1	V_2 (km s^{-1})	σ_2 (km s^{-1})	$(O-C)_2$ (km s^{-1})
44487.472	0.921	104.4	···	34.0	···	−151.6	···	41.2
50526.858	0.057	80.5	6.2	3.6	17	−189.6	2.2	14.5
50527.780	0.394	−117.3	3.5	−4.2	17	131.3	6.8	5.3
50528.845	0.784	−1.8	5.5	1.2	17	−47.6	5.1	17.7
50529.792	0.131	52.3	2.7	3.7	13	−160.3	2.1	−5.4
50530.777	0.491	−122.8	7.1	13.5	17	182.1	7.8	15.6
50531.755	0.849	32.6	6.3	−5.4	17	−148.0	4.6	−11.5
50532.783	0.226	−0.3	6.0	9.4	16	−28.2	7.7	25.5
50533.754	0.581	−125.5	4.4	−3.0	17	159.1	8.4	16.8
50535.766	0.318	−82.8	4.7	−10.8	15	43.4	3.1	−11.2
50910.125	0.378	−98.5	1.7	7.3	9	107.6	2.3	−5.7
50911.086	0.730	−22.1	2.6	18.1	9	−31.6	5.6	−31.0
50911.171	0.761	−29.4	0.4	−10.4	6	−34.3	5.4	3.2
50916.213	0.607	−119.0	4.1	−6.4	10	122.8	5.6	−2.3
50916.990	0.891	58.8	2.5	−0.2	9	−166.8	2.4	6.2
50917.116	0.938	73.9	4.6	−1.5	10	−204.6	3.5	−3.1
50917.257	0.989	79.8	5.4	−3.7	10	−220.4	4.4	−4.8
50917.971	0.250	−26.8	1.8	−0.1	8	−28.0	4.9	−3.8
50918.112	0.302	−59.8	3.8	2.0	8	23.6	2.7	−13.4
50918.249	0.352	−105.3	3.2	−13.0	10	77.5	2.4	−12.4

Table 2. Circular Orbital Elements

Element	Value
P (days)	2.73135 (3)
T_0 (HJD-2,400,000)	50734.286 (11)
K_1 (km s^{-1})	110.1 (28)
K_2 (km s^{-1})	191.4 (48)
$V_{0\ 1}$ (km s^{-1})	−26.4 (19)
$V_{0\ 2}$ (km s^{-1})	−24.6 (32)
$m_1 \sin^3 i$ ($M_\odot$)	4.94 (40)
$m_2 \sin^3 i$ ($M_\odot$)	2.84 (26)
$a_1 \sin i$ ($R_\odot$)	5.94 (15)
$a_2 \sin i$ ($R_\odot$)	10.32 (26)
r.m.s.$_1$ (km s^{-1}) ...	8.4
r.m.s.$_2$ (km s^{-1}) ...	14.2

Note. — Numbers in parentheses give the error in the last digit quoted.

Table 3. Stellar Properties

Property	Primary	Secondary
Spectral Classification ...	O9.5 V	B0.2 III
Relative flux $F/F_1(4000\text{Å})$	1.0	0.96 ± 0.12
$V \sin i$ (km s^{-1})	101 ± 10	132 ± 15
$T_{\rm eff}$ (kK)	32	29
$M/M_\odot$	6.8 – 11.0	3.9 – 6.3
$R/R_\odot$	4.6 – 6.7	4.9 – 7.1
$\log g$	3.9 – 3.8	3.7 – 3.5
$\log L/L_\odot$	4.3 – 4.6	4.2 – 4.5

Note. — The ranges correspond to the values between the underfilling and Roche-filling models.

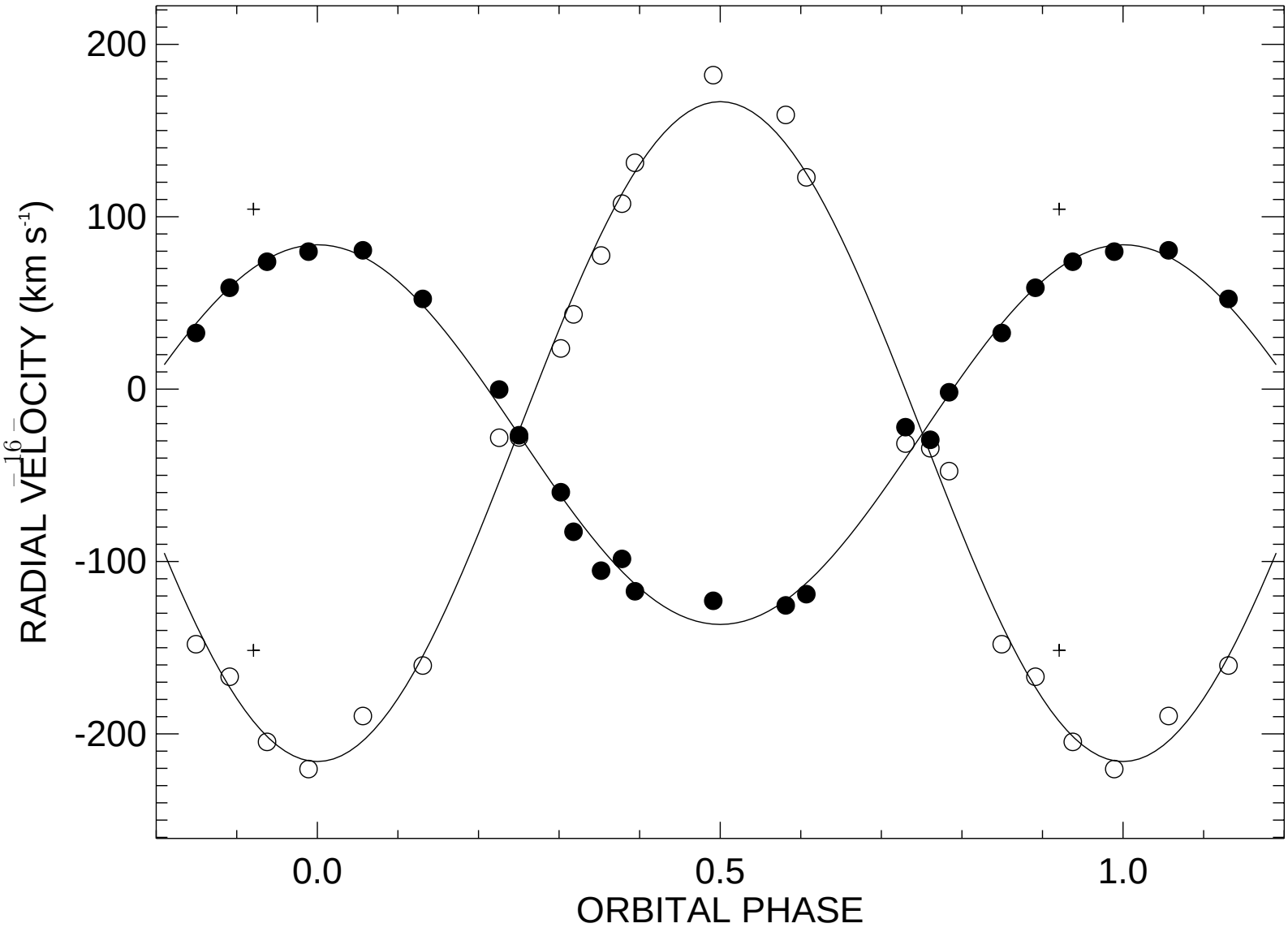
200
100
0
-100
-200
RADIAL VELOCITY (km s-1)
16
0.0
0.5
1.0
ORBITAL PHASE

Fig. 1.—

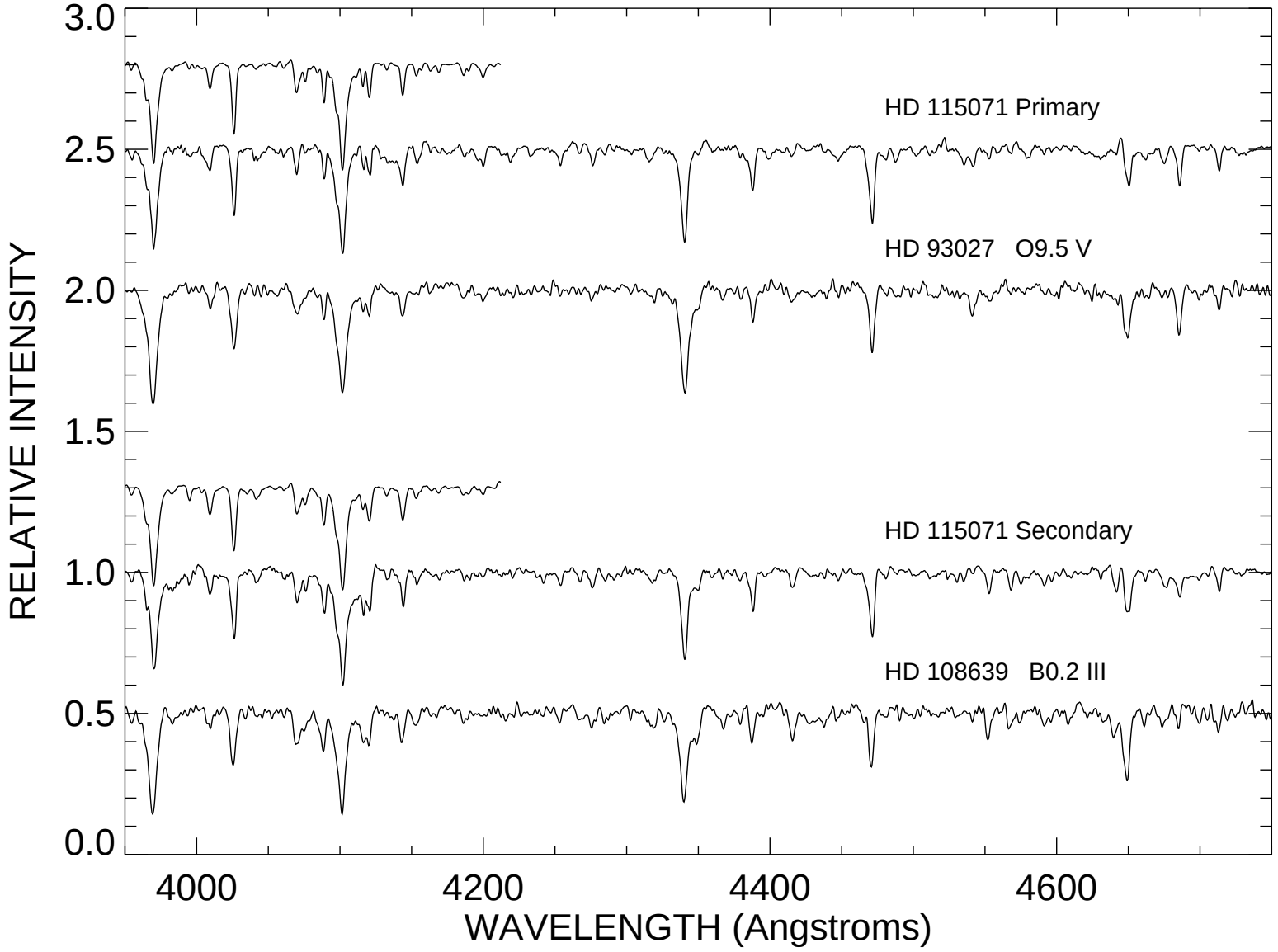
RELATIVE INTENSITY
WAVELENGTH (Angstroms)
HD 115071 Primary
HD 93027 O9.5 V
HD 115071 Secondary
HD 108639 B0.2 III
3.0
2.5
2.0
1.5
1.0
0.5
0.0
4000
4200
4400
4600

Fig. 2.—

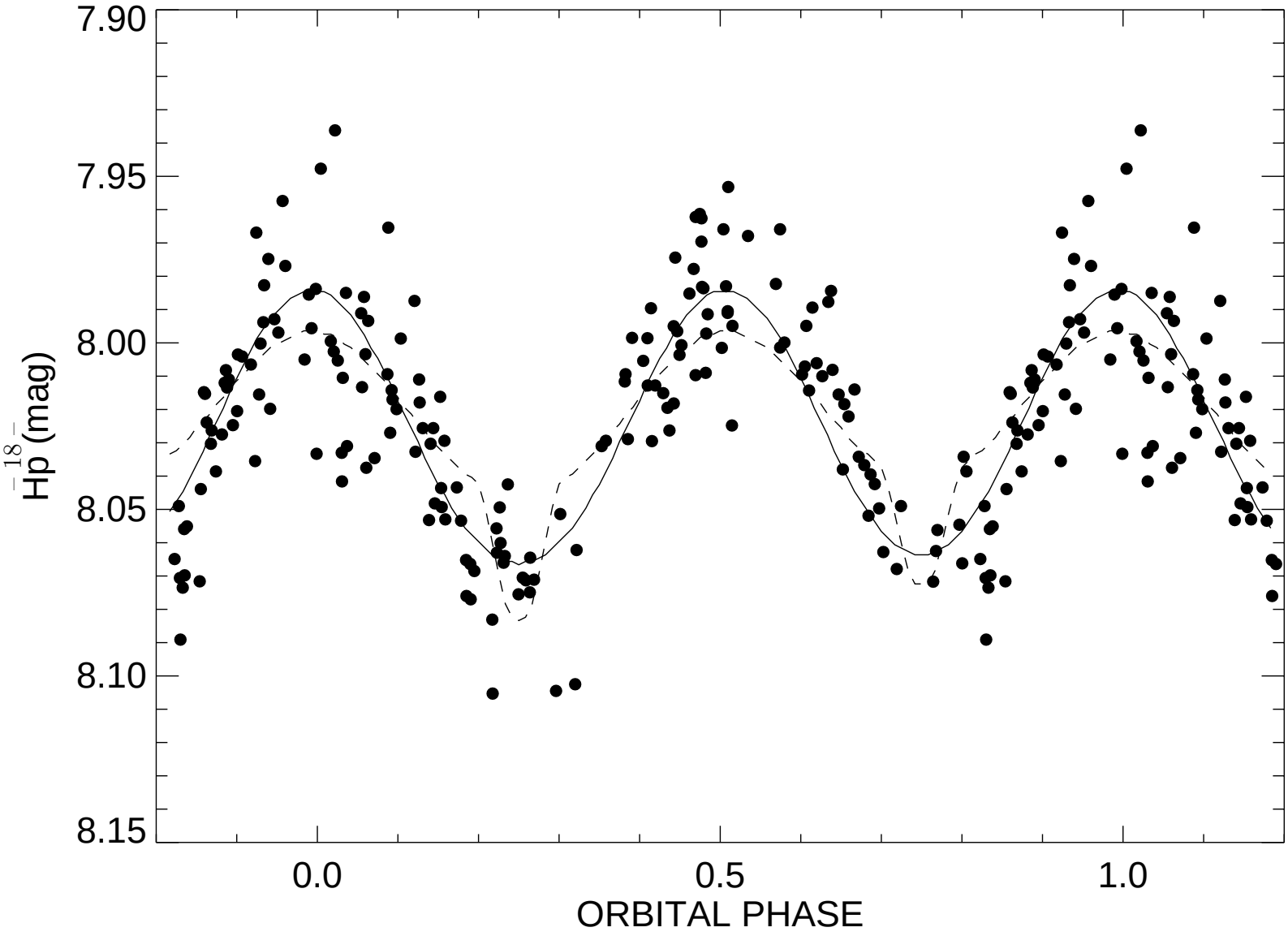

Fig. 3.—